

pubs.acs.org/JACS Article

Synthesis and Characterization of Stable Cu—Pt Nanoparticles under Reductive and Oxidative Conditions

Alexandre C. Foucher, Shengsong Yang, Daniel J. Rosen, Renjing Huang, Jun Beom Pyo, Ohhun Kwon, Cameron J. Owen, Dario Ferreira Sanchez, Ilia I. Sadykov, Daniel Grolimund, Boris Kozinsky, Anatoly I. Frenkel, Raymond J. Gorte, Christopher B. Murray, and Eric A. Stach*



Cite This: J. Am. Chem. Soc. 2023, 145, 5410-5421



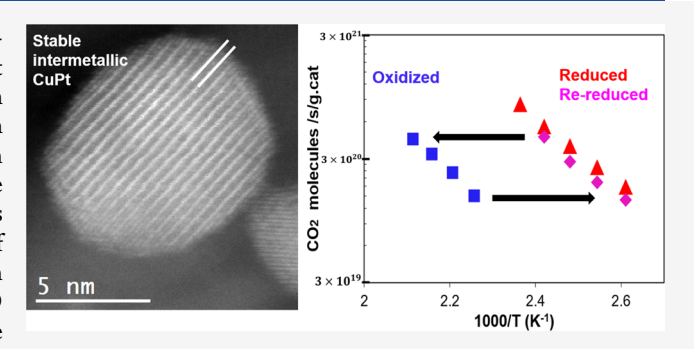
ACCESS

Metrics & More

Article Recommendations

s Supporting Information

ABSTRACT: We report a synthesis method for highly monodisperse Cu–Pt alloy nanoparticles. Small and large Cu–Pt particles with a Cu/Pt ratio of 1:1 can be obtained through colloidal synthesis at 300 °C. The fresh particles have a Pt-rich surface and a Cu-rich core and can be converted into an intermetallic phase after annealing at 800 °C under H₂. First, we demonstrated the stability of fresh particles under redox conditions at 400 °C, as the Pt-rich surface prevents substantial oxidation of Cu. Then, a combination of *in situ* scanning transmission electron microscopy, *in situ* X-ray absorption spectroscopy, and CO oxidation measurements of the intermetallic CuPt phase before and after redox treatments at 800 °C showed promising activity



and stability for CO oxidation. Full oxidation of Cu was prevented after exposure to O_2 at 800 °C. The activity and structure of the particles were only slightly changed after exposure to O_2 at 800 °C and were recovered after re-reduction at 800 °C. Additionally, the intermetallic CuPt phase showed enhanced catalytic properties compared to the fresh particles with a Pt-rich surface or pure Pt particles of the same size. Thus, the incorporation of Pt with Cu does not lead to a rapid deactivation and degradation of the material, as seen with other bimetallic systems. This work provides a synthesis route to control the design of Cu–Pt nanostructures and underlines the promising properties of these alloys (intermetallic and non-intermetallic) for heterogeneous catalysis.

■ INTRODUCTION

Pt-based alloys and intermetallic compounds have been intensively studied because of their potential applications in magnetics, electronics, and particularly in catalysis. 3-7 Although effective, Pt is one of the most expensive catalysts. Therefore, adding inexpensive transition metals into Pt can substantially reduce their cost. Moreover, incorporating transition metals into Pt has been shown to be an effective way to enhance activity and poisoning tolerance in many catalytic processes.^{8–11} Indeed, the mixture of Pt with another transition metal can modify the d-band configuration, yielding a change of adsorption and desorption energy when the samples interact with gaseous molecules. 12,13 Alloying can also lead to different morphologies and shapes that can be advantageous for optimizing the catalytic performance. 14,15 For instance, morphology and facets play a critical role in surface chemistry and hence heterogeneous catalysis. 16-18 Small bimetallic nanoparticles incorporating Pt are common catalysts, as they maximize the surface area of exposed Pt atoms, therefore optimizing it. Many methods are used to produce nanoparticles (such as mechanical milling, sputtering, or chemical vapor deposition), but the sol-gel (solvothermal) method remains the most widely used strategy

to synthesize monodisperse bimetallic nanoparticles. 19 The choice of chemical precursors and solvent can guide the shape of the particles. For instance, halide ions in the solvothermal synthesis of Pt particles help to obtain highly faceted particles.²⁰ Synthesis with metal carbonyl can tune the shape of nanoparticles and yield spheres or cubes, depending on the quantity of precursors and the reaction temperature. 18 Finally, the amount of capping agent added to the solution, such as oleylamine, and the reaction temperature, are crucial to control the size and composition of nanoparticles. 18,21,22 Previous publications have reported promising properties of Pt-based bimetallic particles. For instance, it has been demonstrated that core-shell Pt3Pb-Pt nanoparticles are highly efficient for formic acid oxidation.²³ Pt-Zn particles have been shown to have enhanced poisoning tolerance and comparable activity than pure Pt particles for methanol oxidation. Also, it has

Received: December 22, 2022 Published: February 24, 2023





been shown that Cu-Pt particles outperform pure Pt for lowtemperature propene combustion.²⁴ Improved catalytic properties are the results of unique electronic configuration and morphology in Pt-based bimetallic systems. Finally, core-shell configurations with a Pt-rich skin are also of great interest, as it maximizes the surface area of exposed Pt, with an underlying core modulating the electronic configuration of Pt atoms. Ptbased core-shell particles, with Pt on the surface, have been developed for the electro-oxidation of ethanol or oxidation reduction reaction.^{25,26} Hence, Pt-based bimetallic particles offer tremendous possibilities for stable and highly efficient catalysts. In particular, Pt has been used for CO oxidation reactions, especially in the catalytic converter, to oxidize toxic CO into CO₂. ^{27,28} Hence, the incorporation of Pt with a lowcost metal to reduce the cost of catalyst for CO oxidation appears as an appealing strategy.

To this end, we report the synthesis of highly monodisperse Cu-Pt alloy nanocrystals. We achieved control over the size of Cu-Pt particles with different diameters and showed that the Cu-Pt alloy nanocrystals can be prepared with a stoichiometry of Cu/Pt = 1:1. The fresh particles have core-shell structure with a Pt-rich surface that can be converted into an intermetallic phase with thermal annealing. We showed that the fresh particles, with a high Pt concentration on the surface, are stable under O₂ at temperatures up to 600 °C. Thus, a thick Pt-rich shell can prevent oxidation of a Cu-rich core and subsequently the migration of Cu to the surface through the Kirkendall effect. The fresh nanocrystals can be subsequently converted into CuPt intermetallic nanocrystals by exposing them to an inert atmosphere at 800 °C. We then demonstrated the great stability and high activity for CO oxidation of the intermetallic phase during a redox cycle performed at 800 °C. Detailed in situ scanning transmission electron microscopy (STEM) and in situ X-ray absorption spectroscopy (XAS) investigations were performed in parallel to CO oxidation measurements. The activity for CO oxidation of the CuPt intermetallic phase was higher than pure Pt particles of similar size and the fresh core-shell Cu-Pt sample. The intermetallic phase is also very stable and very resistant to redox conditions at 800 °C. Full oxidation of Cu was prevented after exposure to O2 at 800 °C. The activity of the particles was only slightly reduced after exposure to O2 at 800 °C but could be fully recovered after re-reduction at 800 °C. This underlines the fact that a bimetallic structure with Cu can be a stable and efficient catalyst, and the consequences of Cu oxidation can be reversed.

EXPERIMENTAL METHODS

For the synthesis of nanostructures, $\text{Cu}(\text{acac})_2$ (Cu(II) acetylacetonate $\geq 97\%$ purity) and $\text{Pt}(\text{acac})_2$ ($\geq 97\%$ purity) were purchased from Sigma-Aldrich. Oleylamine (Olam, $\geq 70\%$ purity), benzyl ether (BE, $\geq 98\%$ purity), oleic acid (OAc, $\geq 99\%$ purity), and *tert*-butylamine borane complex (TBAB, $\geq 97\%$ purity) were also purchased from Sigma-Aldrich.

All syntheses of nanostructures were performed using the solvothermal method. ²⁹ Briefly, 9.0 nm (large) Cu–Pt nanocrystals with a 1:1 ratio were synthesized using 0.052 g of Cu(acac)₂ and 0.080 g Pt(acac)₂. The precursors were mixed with 10 mL of benzyl ether, 7.36 mL of oleylamine, and 1.25 mL of oleic acid. The solution was first placed under vacuum at an elevated temperature (95 °C for 1 h) under constant stirring to remove traces of water. Then, the solution was rapidly heated under N₂ (15 °C/min) and kept at a high temperature for 1 h. The solution was then slowly cooled down under N₂. Hexane and isopropanol were added to the mixture before

centrifuging at 8000 RPM for 5 min. The particles were then redispersed in hexane.

The addition of 100 mg of TBAB at $170~^{\circ}$ C when the mixture's temperature is elevated yields 3.2 nm (small) Cu—Pt nanoparticles.

In addition, small Cu–Pt particles with a Cu/Pt ratio of 3:1 can be obtained using the same recipe for large Cu–Pt particles with a reaction temperature of 210 $^{\circ}$ C maintained for 30 min. If the reaction is stopped after 10–15 min, then Cu–Pt nanowires are obtained, with a Cu/Pt ratio of 3:1 (Figures S2 and S3).

Pure Pt particles were synthesized for comparison with the catalytic properties of large CuPt particles. The synthesis was the same as for large CuPt particles, except that no Cu precursor was added, but only 0.080 g of Pt(acac)₂. The diameter of the pure Pt particles was 8 ± 2.1 nm.

Transmission electron microscopy (TEM) was performed with a JEOL1400 TEM at 120 kV. STEM, energy-dispersive X-ray spectroscopy (EDS), and electron energy-loss spectroscopy (EELS) were performed with a JEOL NEORM operating at 200 kV with a convergence angle of 27 mrad. For STEM imaging and EDS, the probe current was 150 pA, and the camera length was 4 cm. For EELS, the probe current was 500 pA, and the camera length was 2 cm to maximize the signal-to-noise ratio. A K2-IS camera operating in the Summit mode, provided by Gatan Inc., was used to collect the EELS spectra, using a 5 mm collection aperture on the Gatan imaging filter (GIF). Crystal structures were also investigated through X-ray diffraction patterns and obtained using a Rigaku Smartlab diffractometer with Cu K α radiation of $\lambda = 1.5418$ Å. To accurately measure the Cu/Pt ratio in the synthesized Cu-Pt nanocrystals of different compositions, we performed inductively coupled plasma optical emission spectroscopy (ICP-OES) on a SPECTRO GENESIS ICP spectrometer.

In situ STEM analysis was performed with a JEOL NEOARM operating at 200 kV. An environmental holder manufactured by Hummingbird Scientific was used to perform in situ gas-heating experiments. $^{30-32}$ The sample was enclosed into a microcell with two electron-transparent SiN windows. The cell also contained a micro coil for temperature control. Gas flow was 5 sccm, and only pure gases (99.999% purity) were used (H₂, O₂, or N₂ to purge the system). Flow and temperature were controlled with a gas delivery system and software provided by Hummingbird Scientific. For all in situ STEM experiments, particles were deposited on amorphous carbon (instead of Al₂O₃) to avoid loss of contrast and maximize imaging quality in high-angle annular dark-field (HAADF)-STEM mode. Ligands were removed by calcination under O₂ at 250 °C for 5 min. The short treatment did not damage the carbon support or the particles.

In situ XAS was performed at the microXAS beamline (X0SLA) at the Swiss Light Source (SLS) of the Paul Scherrer Institute (PSI). Data for Cu K and Pt L₂ edge were collected in fluorescence mode with Silicon Drift Detectors. The flux was $2\times 10^{12}~\rm ph/s/400~mA$, and the spot size was approximately $10\times 10~\mu m^2$. The sample was enclosed in the same environmental holder used for in situ STEM, with the same flow rates, gases, and temperatures. The Pt L₂ edge was analyzed instead of the Pt L₃ edge, as the holder contained tungsten. Hence, the Pt L₃ edge (11.5637 keV) overlapped with W L₂ edge (11.5440 keV).

Catalytic properties of Cu–Pt (CuPt) nanocrystals supported on Al_2O_3 toward CO oxidation were tested and compared to pure Pt nanoparticles. The γ -alumina was first exposed to 900 °C for 24 h to stabilize the structure and avoid substantial changes of the support during catalysis at elevated temperatures. We chose Al_2O_3 , as it is completely inert for CO oxidation, enabling us to measure the activity of the particles, independent of support effects. The dispersed particles in hexane were mixed with a finely ground powder of γ -Al $_2O_3$ and put in an ultrasonic bath for 1 h. The sample was then centrifuged and dried to obtain a powder of supported catalyst. For all CO oxidation measurements in this study, plasma cleaning with argon was performed for 20 min before calcination under air at 500 °C for 2 min to remove ligands. To compare the activity of the different samples for CO oxidation, we used a gas hourly space velocity (GHSV) of 36,000 mL h $^{-1}$ g $^{-1}$ catalyst. CO oxidation was performed with 25 torr

of CO, 12.5 torr of O_2 , and 722.5 torr of He. The weight loading of Pt was 0.5% for all samples. All formation rates ($CO_2/s/g.cat$) only encompass the amount of Pt (g.cat of Pt) and exclude Cu.

Metal dispersions were estimated using standard chemisorption measurements with CO at room temperature (20 °C). The sample was first oxidized at 300°C in air for 10 min and then reduced in pure $\rm H_2$ at 300°C for 30 min before evacuation and cooling. Dispersions were calculated from the cumulative amount of CO adsorption up to 2 Torr, assuming that the stoichiometry of Pt/CO is 1.³⁴ CO does not adsorb on Cu.³⁵

RESULTS AND DISCUSSION

The reaction under an inert atmosphere at 300 $^{\circ}$ C for 30 min yields large Cu–Pt particles with an average diameter of 9.0 \pm 1.1 nm and a Cu/Pt ratio of 1:1 (Figure 1a). This

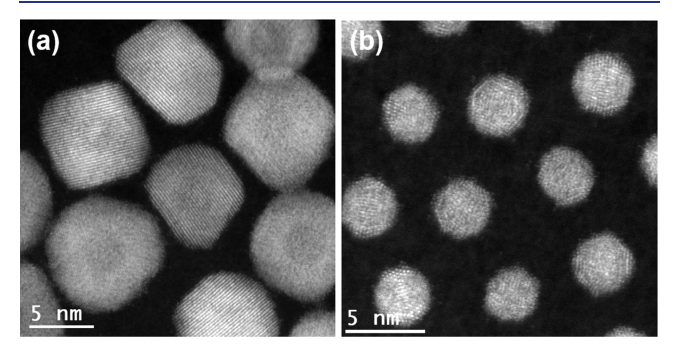


Figure 1. STEM images of Cu-Pt nanocrystals. (a) HAADF-STEM image of 9.0 nm Cu-Pt particles, (b) HAADF-STEM image of 3.2 nm Cu-Pt particles.

stoichiometry is consistent with the initial quantity of precursors. If TBAB is added, the same reaction conditions yield 3.2 ± 0.27 nm Cu–Pt particles with a Cu/Pt ratio of 1:1 (Figure 1b). Additional images with a lower magnification are provided in Figure S1.

It should be noted that the as-synthesized samples do not have an intermetallic structure. Conversion into an intermetallic arrangement can be achieved after annealing at 800 °C for at least 30 min. The table below (Table 1) shows the nomenclature of the samples investigated in this work. We used "CuPt" to indicate intermetallic phase and "Cu-Pt" for non-intermetallic phase. No substantial change in size was observed after particles were converted into intermetallic alloys.

In addition, we noticed that changes in synthesis parameters can provide flexibility in the design of Cu–Pt structures. If the synthesis is performed at 210 °C (without TBAB), then we obtained small Cu–Pt nanoparticles with a Cu/Pt ratio of 3:1 and with long nanowires as a byproduct. We also performed the synthesis at 210 °C by collecting a small fraction of the

solution every 5 min after the beginning of the reaction. Results are summarized in Figure S3 and show the initial formation of nanowires after 10 min of synthesis, which are transformed into nanoparticles when the reaction is performed for at least 25 min. This shows the large range of available nanostructures that can be obtained with the recipe reported in this work.

For the rest of this study, we decided to mostly focus on the small Cu–Pt and large Cu–Pt particles synthesized at 300 $^{\circ}$ C, which have a Cu/Pt ratio of 1:1. The particles were analyzed with aberration-corrected STEM imaging combined with EELS and EDS to obtain a precise understanding of the spatial distribution of Cu and Pt within individual particles. The results are summarized in Figure 2. Only freshly synthesized particles were investigated, and no thermal pretreatment was performed. In both cases, it was possible to distinguish a Curich core covered by a thick Pt-rich structure (Figure 2b,f). The high concentration of Pt on the surface seems advantageous, as Pt is the precious metal that we try to optimize for heterogeneous catalysis.

Additionally, it was not possible to distinguish a layer of Cu or Cu oxide on the surface of the particles, even after 6 months in solution. This indicates the stability of the Cu–Pt system as Cu tends to segregate to the surface and oxidize when it forms an alloy, especially since its surface energy for many facets is low. ^{36–38} EELS of the Cu L_{2,3} spectra (Figure 2c,g) indicates no oxidation of Cu into CuO or Cu₂O, as the edge has the characteristic shape for reduced Cu. If CuO was present, we should see sharp peaks called "white lines" at 931 and 951 eV loss. ^{39,40} If Cu₂O was present, the signal should display undulations after the front edge. ³⁹ Additionally, EELS of the O K edge at 529 eV loss and EDS did not detect the presence of oxygen in the particles (Figure S4). Thus, we conclude that the particles are not oxidized, and exposure to air or suspension into hexane with alcohol traces does not cause rapid oxidation.

No intermetallic phase could be distinguished in fresh samples (small and large particles), especially since the atomic resolution images with HAADF-STEM do not suggest a regular ordering of Cu and Pt. Indeed, since $Z_{\rm Cu}=29$ and $Z_{\rm Pt}=78$, an intermetallic solution would be clearly visible, as the brightness of the atoms is proportional to $Z^{1.6}$. Thus, we conclude that the freshly synthesized samples are alloyed with a Cu-rich core and a Pt-rich surface.

Then, we investigated the catalytic properties of small and large fresh Cu-Pt particles after the removal of ligands. The objective was to understand whether the alloyed Cu-Pt particles could resist oxidative conditions even if the particles were not converted into robust intermetallic phases. The samples were reduced and oxidized at 400 °C. Two reductions and two oxidations were performed, and the data shown in

Table 1. Nomenclature and Description of the Samples Mentioned in This Work

| sample's nomenclature | average diameter (nm) | Cu/Pt ratio | synthesis temperature (°C) | description |
|--------------------------|-----------------------|----------------|---|---|
| large Cu-Pt particles | 9.0 | 1:1 | 300 °C | non-intermetallic alloy |
| large CuPt particles | 9.0 | 1:1 | 300 °C | intermetallic alloy (annealed in an N_2 environment at 800 $^{\circ}\text{C}$ for 30 min) |
| small Cu-Pt particles | 3.2 | 1:1 | $300~^{\circ}\text{C}$ with TBAB injected at $170~^{\circ}\text{C}$ | non-intermetallic alloy |
| small CuPt particles | 3.2 | 1:1 | $300~^{\circ}\text{C}$ with TBAB injected at $170~^{\circ}\text{C}$ | intermetallic alloy (annealed in an N_2 environment at 800 $^{\circ}\text{C}$ for 30 min) |

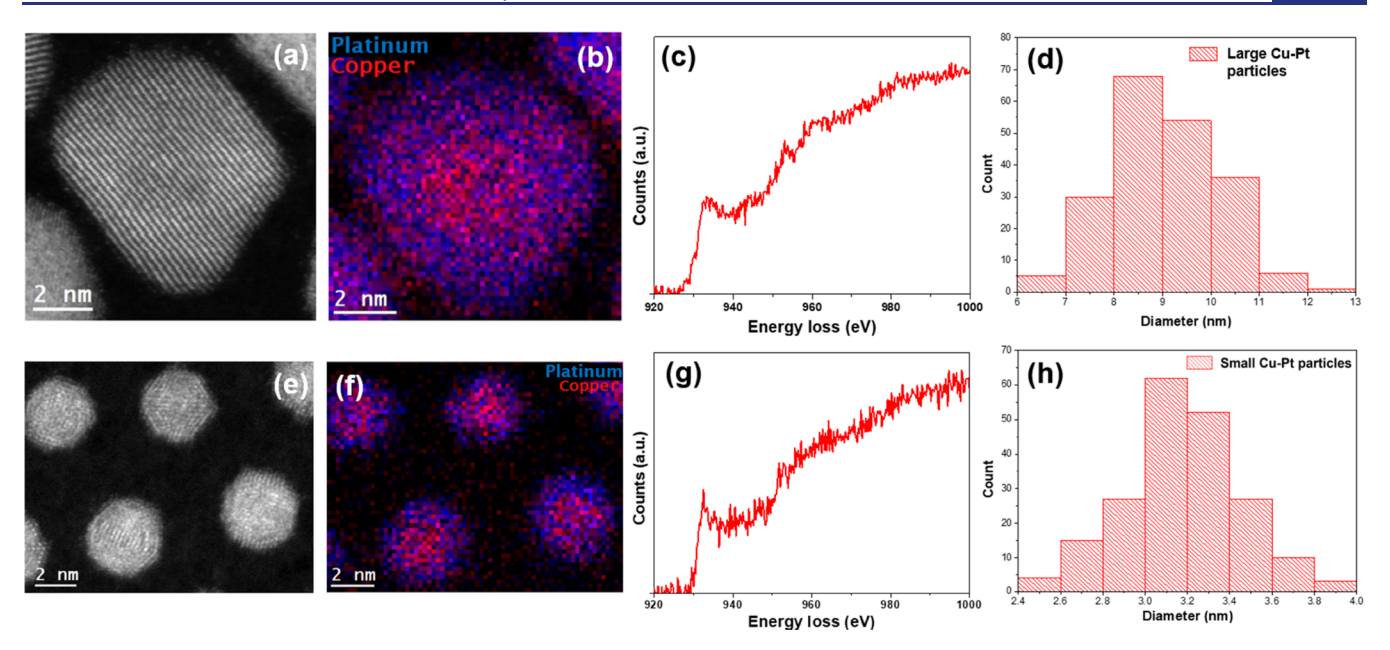


Figure 2. STEM-EELS and EDS analysis of the fresh large and small nanoparticles. (a) HAADF-STEM image of a representative large Cu-Pt nanoparticle. A dimmer contrast in the center indicates the presence of more Cu than on the edges. (b) Corresponding and combined EDS maps for Cu and Pt showing a Cu-rich core enveloped in a thick Pt-rich shell. (c) Cu $L_{2,3}$ EELS edge from the surface of the particles, showing no oxidation of Cu. (d) Particle size distribution for 200 large particles. (e) HAADF-STEM image of representative small Cu-Pt nanoparticles. (f) Corresponding and combined EDS maps for Cu and Pt, showing a Cu-rich core enveloped in a Pt-rich shell. (g) Cu $L_{2,3}$ EELS edge from the surface of the particles, showing no oxidation of Cu. (h) Particle size distribution for 200 small particles.

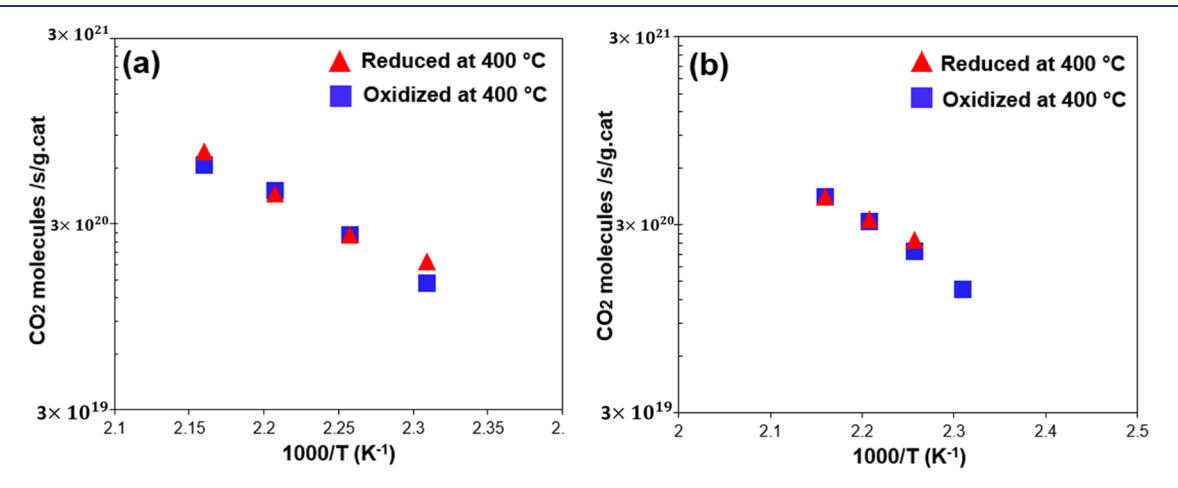


Figure 3. Investigation of the stability of large (9.0 nm) and small (3.2 nm) particles during a mild redox cycle at 400 °C (a) Steady-state differential for CO oxidation rate with 25 torr of CO and 12.5 torr of O_2 with 9.0 nm Cu-Pt particles as the catalyst. 0.1 g of Cu-Pt/Al₂O₃ was used. (b) Steady-state differential for CO oxidation rate with 25 torr of CO and 12.5 torr of O_2 with 3.2 nm Cu-Pt particles as the catalyst. 0.1 g of Cu-Pt/Al₂O₃ was used. In both cases, the catalyst is still active, and oxidation does not substantially alter the catalytic properties after a reduction.

Figure 3 indicate the activity after the second reduction and the second oxidation.

The catalysts are still active after two redox treatments, and the activity does not change substantially between reduction and oxidation. This indicates minor changes in composition in the Cu–Pt particles during the redox cycle. It is surprising to see no substantial drop in activity after cycling, especially since Cu migrates easily to the surface upon exposure to O₂-rich environments. This has been shown in other publications about bimetallic particles with Cu.^{22,31} Upon exposure to oxygen at high temperatures, Cu migrates to the surface and forms Cu oxide, which covers the second transition metals. In our case, it seems that the Pt-rich surface prevented the migration of Cu to the surface, which allowed Cu–Pt particles

to remain active after the cycle. Finally, it is interesting to notice that the rates for CO oxidation are similar for small and large particles. One could have expected small particles to be more active, as the surface area is larger. We speculate that the highly faceted surface of large particles, with wide planar surfaces, may boost the rate and therefore offset the smaller surface area compared to small particles.

Ultimately, we performed an *in situ* STEM experiment to understand changes in the structure under realistic conditions. The particles were deposited on amorphous carbon and not on Al_2O_3 . A brief exposure to O_2 at $250^{\circ}C$ for 5 min was performed to remove ligands without damaging the carbon support. The sample was first exposed to pure H_2 up to 400 °C. Then, the sample was cooled down to room temperature

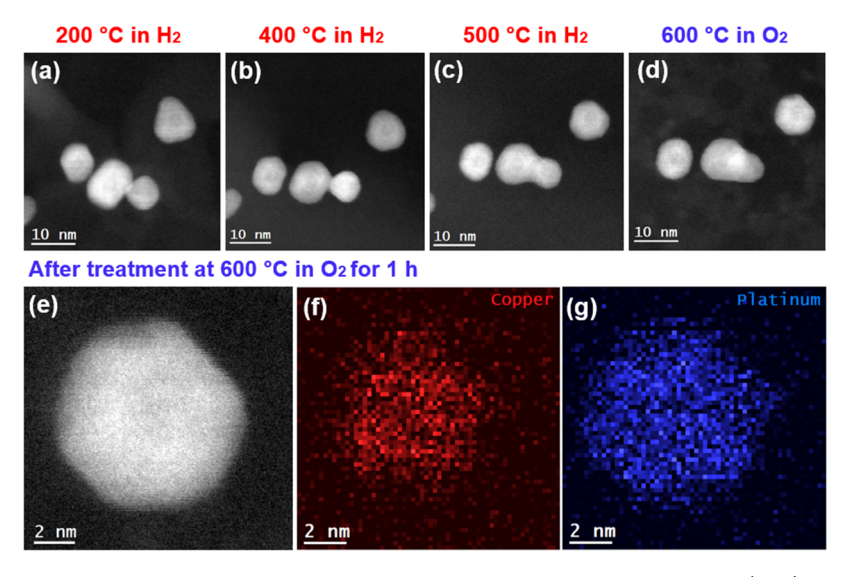


Figure 4. In situ STEM-HAADF analysis of large Cu-Pt particles shed light on the stability of the sample. (a-d) Reduction and oxidation of the sample at elevated temperatures. Images were taken after at least 30 min at the indicated temperatures and gases. A dimmer brightness in the center of the particles at the end of the experiment proves the resistance of the Cu-rich core. (e-g) STEM image and corresponding EDS maps of a particle after the end of the oxidation step at 600 °C. Pt is still strongly present on the surface. The Cu-rich core is also visible.

under N_2 , and O_2 was provided. The final temperature for the O_2 treatment was gradually increased to 600 °C. The samples were also deposited on amorphous carbon instead of Al_2O_3 to increase the visibility of the particles with *in situ* STEM. Al_2O_3 is heavier than amorphous carbon; hence, it will be more challenging to see the particles with HAADF-STEM imaging. Furthermore, minimizing the effect of the support on the imaging and spectroscopy measurements is critical for detecting the migration of Cu to the surface. The results of the *in situ* analysis are summarized in Figure 4. All images were taken after at least 30 min of exposure to the indicated gas and temperature.

The particles are stable at high temperatures under O₂ or H₂. In fact, Cu tends to sinter very easily at elevated temperatures, but the Cu-Pt phase prevents sintering or morphology changes commonly seen in Cu nanostructures. Some moderate sintering is detected after prolonged exposure to high temperature for particles that were initially quite close to each other (Figure 4c). It is also possible to notice occasional restructuring of facets during redox cycling. For instance, the particle on the top right in Figure 4 was initially triangular and became hexagonal at the experiment's end. 36,42 However, one can notice that the particles remain faceted during the whole cycle under reductive or oxidative conditions. Mild sintering and facet reconstruction may explain the slight decrease in activity during cycling. The Cu-rich core in the particles is visible at the beginning of the experiment and remains during the redox cycling. This can be seen in the EDS data in Figure 4. In Figure 4d, the morphology of the particles remained unchanged under oxidative conditions. These results are in contrast to the behavior of pure Cu particles under harsh oxidative conditions: Cu quickly oxidizes a form a hollow structure through the Kirkendall effect. 43-45

Finally, EELS analysis was performed on the Cu $L_{2,3}$ edges at 931 and 951 eV loss to determine if Cu became oxidized after 1 h of exposure to O_2 at 400 °C. The signal for oxygen could not be used with the *in situ* experiment as traces of SiO_2 are present in the cell and the windows enclosing the sample. Thus, we relied on a fingerprinting approach by looking at the

shape of the Cu L_{2,3} edges.^{39,46} The results are shown in Figure S5. In most cases, no sign of Cu oxidation was detected as the edges remained flat and did not have characteristic peaks for Cu oxide. In some particles, it was possible to detect modest white lines suggesting partial oxidation of Cu in the sample.³⁹ Thus, we conclude that Cu remains difficult to oxidize in large non-intermetallic Cu-Pt particles, explaining the stable catalytic performance described in Figure 3. The Cu-rich core remains well embedded in the thick surface and Pt-rich phase. Cu has difficulty migrating within the particles and is not able to accumulate on the surface. In fact, migration of Cu to the surface, followed by oxidation, is a common problem in alloyed materials, as Cu has a low surface energy. 47,48 High temperatures combined with an O2-rich atmosphere favor quick degradation of bimetallic samples containing Cu, but we believe the unique configuration of these Cu-Pt particles either prevents or strongly hinders such an outcome.

After this analysis at low temperatures, the small and large particles are then converted into an intermetallic solution upon annealing at elevated temperatures for 30 min under N_2 at 800 °C. XRD and STEM data are provided in Figures S6 and S7 and show the effective conversion of CuPt particles into an intermetallic phase. This is consistent with the phase diagrams of the Cu–Pt system reported in a previous publication. ⁴⁹

Catalytic properties of CuPt particles are then investigated during CO oxidation. To this end, we compared small and large CuPt particles as well as Pt particles with a diameter of 8 nm.

The results of the catalytic testing are summarized in Figure 5. Arrhenius plots are presented for the three samples in a temperature range of 110–160 °C. 50,51 Activation energies were calculated assuming the same rate expression for all samples and are provided in Table S1. Large CuPt particles were slightly more active than small CuPt particles, which was surprising as small particles have a higher surface area. Standard CO chemisorption was performed on the two samples, and the dispersion was calculated (Table 2). The results confirm the higher activity of large CuPt particles compared to Pt particles with a similar size. Surprisingly, the

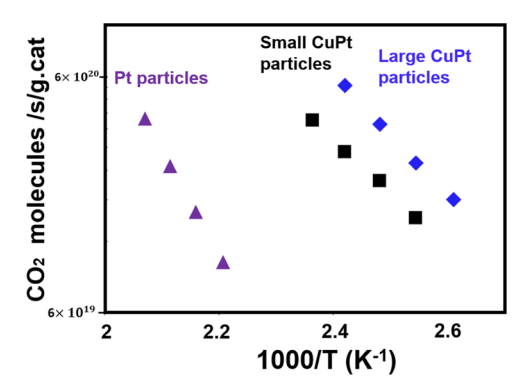


Figure 5. Arrhenius plot shows catalytic activity in the 175–275 °C range. Large 9.0 nm CuPt particles had the highest activity at low temperatures, even though the surface area was lower compared to smaller particles. Both alloys are more active at low temperatures than pure Pt particles. We speculate that the particular morphology of 9.0 nm particles shown by the STEM analysis is responsible for enhanced properties.

Table 2. Results of CO Chemisorption for Large and Small Intermetallic CuPt Particles^a

| materials | dispersion according to CO chemisorption, assuming Pt/CO is 1:1 | calculated dispersion for Pt particles with the same size as the CuPt system |
|----------------|---|--|
| 9.0 nm CuPt | 17.3% | 12% |
| 3.2 nm CuPt | 14.3% | 33% |

^aThe results are compared to Pt particles with the same size.

dispersion of large CuPt particles (17.3%) was higher than Pt particles of the same size (12%), which suggests a better absorption of CO molecules on the surface of large CuPt systems. In contrast, small CuPt particles had a lower dispersion (14.3%) compared to the calculated dispersion of Pt particles with the same size (33%). This explains why small CuPt particles did not outperform large CuPt particles when CO oxidation was tested.

One can also notice that CuPt particles do not seem to obey the same dispersion curve as Pt. In fact, it is known that with CO oxidation on pure Pt, rates are strictly proportional to the Pt surface area.⁵² Hence, CuPt alloys do not fit that same rate versus dispersion curve observed with Pt.

Additionally, the 9.0 nm CuPt particles appear to be more active at low temperatures than the 8.0 nm Pt particles synthesized in this work. The STEM images showed facets on the 9.0 nm CuPt nanoparticles, which could explain the enhanced activity. In fact, facets and surface orientations play a critical role in heterogeneous catalysis, as they define the electronic configuration at the surface of the metal. Different orientations and facets will modify the adsorption and desorption energies, leading to modified catalytic properties. We also repeated twice the CO oxidation measurement on different batches of CuPt and pure Pt samples, and we obtained the same results. Additionally, we also compared the CuPt samples with a commercial Pt/Al₂O₃ sample, and we also measured activity at lower temperatures for the alloy (Figure S8). A full comparison between Pt samples and CuPt particles will be provided in future work, as the comparison of catalytic properties between monometallic and bimetallic samples is sometimes challenging. A range of factors can explain the catalytic properties of bimetallic samples and have been under debate. This work aims to show that the incorporation of Cu into Pt does not necessarily passivate Pt used for catalytic reactions. It also underlines interesting properties of intermetallic structures and the impact of morphology on catalysts.

Finally, one should notice that all samples are more active than pure Cu particles deposited on ${\rm Al_2O_3}$. The Arrhenius plot for pure Cu particles in a previous work showed high activity for Cu at high temperatures, in the 230–280 °C range. ²² This is also consistent with previous publications as Cu is not considered an efficient catalyst for CO oxidation. ^{53–58}

It is also very interesting to notice an increase of activity upon conversion of the large Cu–Pt particles into an intermetallic solution (Figure 6a). The activity of fresh 9.0 nm Cu–Pt particles is only slightly higher than the measured activity for pure Pt particles. After exposure to $\rm H_2$ at 800 °C for 1 h, the sample becomes more active as the Arrhenius plot is shifted to a lower temperature range. The formation of an intermetallic solution may yield a unique electronic configuration more favorable for CO oxidation compared to the Cu–Pt alloy before annealing. $^{56-58}$ It should be noted that the activity of pure $\rm Pt/Al_2O_3$ did not change after the same treatment, as the sample was already fully reduced. We also performed some calculations using density functional theory (DFT) with a Vienna Ab initio Simulation Package. 59 CO calculations were corrected for a singlet—triplet correlation

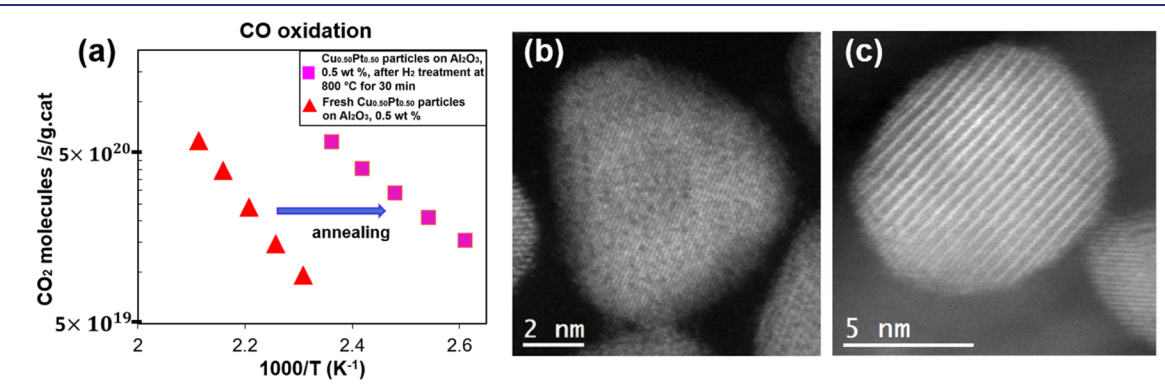


Figure 6. (a) Arrhenius plot for the 9.0 nm particles after calcination and after a thermal treatment to convert the Cu-Pt particles into an intermetallic solution (CuPt). The activity increases upon thermal treatment. (b) HAADF-STEM image of the sample before treatment, with no intermetallic solution. (c) HAADF-STEM image of the sample after treatment, showing the intermetallic ordering.

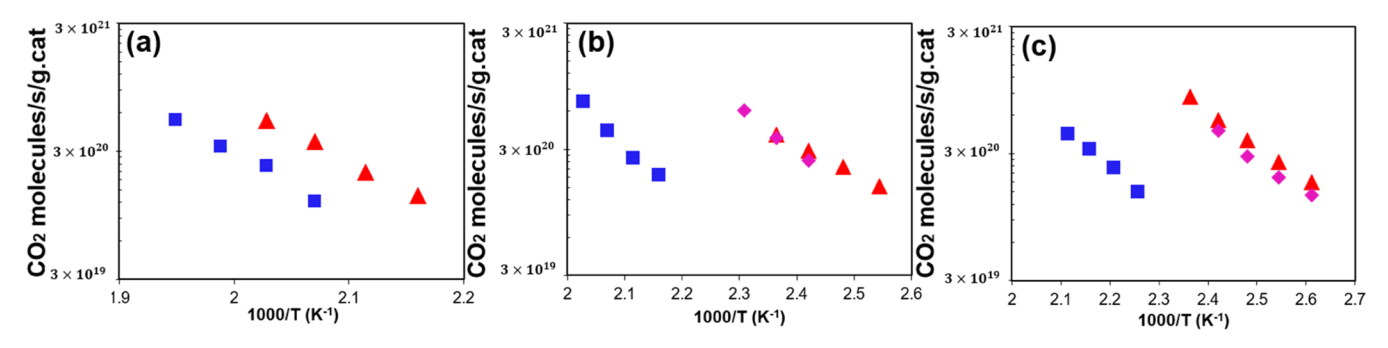


Figure 7. CO conversion into CO_2 at elevated temperatures was used to investigate the stability of small and large intermetallic CuPt particles. The CuPt particles have a higher activity compared to 8.0 nm Pt particles upon reduction at 800 °C. The CuPt samples can be regenerated after oxidation by exposure to H_2 at 800 °C. (a) Pure Pt particles after oxidation (blue square) and reduction (red triangle). (b) Small CuPt particles' reduction (red triangle), oxidation (blue square), and re-reduction (pink diamond). (c) Large CuPt particles' reduction (red triangle), oxidation (blue square), and re-reduction (pink diamond).

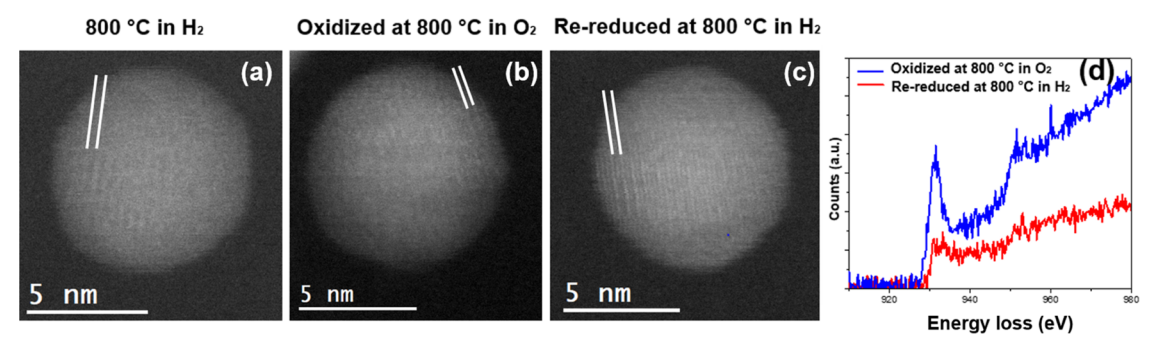


Figure 8. CuPt Particle tracked with *in situ* STEM during oxidation and reduction at 800 °C. (a) After 1 h reduction at 800 °C. The intermetallic structure is visible and underlined by the white lines. (b) After 1 h oxidation at 800 °C. No segregation of Cu is visible. One can still distinguish the intermetallic structure. (c) After 1 h re-reduction at 800 °C. (d) EELS analysis proving oxidation of Cu after exposure to O₂ at 800 °C.

error, and ${\rm O/O_2}$ adsorption calculations were corrected for Perdew–Burke–Ernzerhof (PBE) over binding of CO. The initial calculations are presented in Figure S9 and show a potential stable site of CuPt(111) surfaces, which could explain the high activity. A comprehensive DFT study will be published in a future publication. Previous DFT studies have pointed to the higher activity of Cu₃Pt and CuPt alloys for CO oxidation. This is due to O–O bonds being broken with a lower kinetic barrier with CuPt(111) compared to pure Pt. Hence, it allows better interaction with CO and adsorbed O₂ and ultimately leads to lower kinetic barriers.

We then investigated the stability of small and large CuPt particles. First, the analysis is performed on particles exposed to 800 °C in a 10% H₂ atmosphere balanced with He for 1 h to form an intermetallic solution. The sample was then exposed to 800 °C in a 10% O₂ atmosphere balanced with He for 1 h. The samples were ultimately re-reduced at 800 °C for 1 h with a 10% H₂ atmosphere with He. Pure Pt particles with an average diameter of 8 nm were also synthesized and exposed to the same treatment as the CuPt samples for comparison. The results are summarized in Figure 7. Images of the particles on γ-Al₂O₃ are shown before and after treatment in Figure S10. Figure 7a shows the activity of pure Pt particles after reduction (red triangle) and oxidation at 800 °C (blue square). As expected, the activity is lower after oxidation due to the formation of PtO or PtO2 on the surface of the particles, caused by the harsh oxidation conditions. Figure 7b shows the activity of small CuPt particles after the first reduction (red triangle), after oxidation (blue square), and after re-reduction (pink diamond). Oxidized CuPt particles have an activity comparable to Pt particles after oxidation. However, the reduced sample displays strong activity after the first and second reduction cycles. Thus, the small CuPt particles can be regenerated after exposure to harsh oxidation conditions. Figure 7c shows the same experiment for large CuPt particles with similar conclusions. Large CuPt particles can be regenerated after re-reduction. We also conclude that small and large CuPt particles have a higher activity for CO oxidation in the 110-160 °C range compared to 8.0 nm Pt after a thorough reduction. We also compared our results to the CO₂ formation rate (TOF) on Pt(100) and Pt/silica surfaces provided in a previous publication.⁵² Those authors showed that CO oxidation rates per area on pure Pt are independent of the surface structure or particle size. They also showed that the activation energy of the reaction is equal to the enthalpy of CO adsorption under the conditions in which we worked due to the fact that the reaction is limited by O2 adsorption onto a CO-saturated surface. We found that CO oxidation rates on the CuPt intermetallic particles after reduction were a factor of 5 higher than what would be expected for pure Pt. The activation energy on CuPt was also much lower than what we found for pure Pt. This suggests that the heat of adsorption of CO is weaker on the alloy, so rates are higher because the surface is not poisoned by CO.

To better understand the stability of CuPt nanocrystals, we performed *in situ* STEM-EDS analysis on large particles (Figure 8). We chose the large nanoparticles as they are easier to see with *in situ* STEM. The sample is enclosed in a small microreactor between two SiN₃ windows. This causes a drop in imaging and EDS quality; hence, it is preferable to analyze the

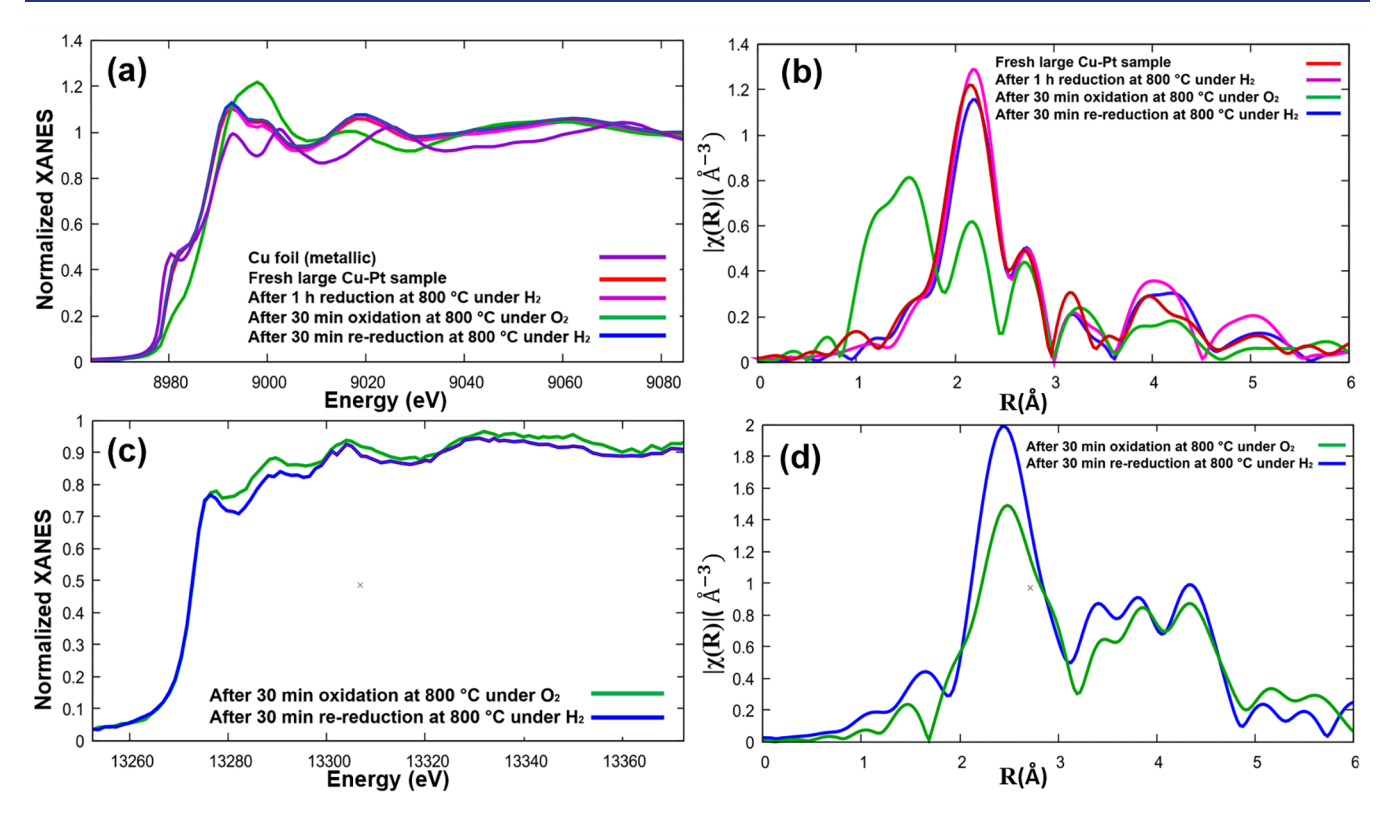


Figure 9. In situ XAS data collected during reduction, oxidation, and re-reduction at 800 °C. (a) XANES of Cu-K edge showing changes in the valence state of Cu. XANES region of bulk Cu is shown for comparison. (b) FT-EXAFS data for Cu-K edge. (c) XANES of Pt L2 edge. (d) FT-EXAFS data for Pt L2 edge. No change in the valence state could be detected for Pt.

large particles to obtain better data quality. For the *in situ* experiment presented in this section, the fresh CuPt particles had a diameter of 8.6 ± 1.3 nm (a bit smaller than the 9.0 ± 1.1 nm diameter observed on average). After annealing, the diameter was 8.8 ± 1.9 nm.

The particles were exposed to H₂ at 800 °C for 1 h, then oxidized with O2 at 800 °C for 1 h, and finally re-reduced with H₂ at 800 °C. No substantial segregation of Cu on the surface could be distinguished. The strong stability is remarkable, as not all intermetallic structures are always resistant to harsh environments. 53,63,64 It is even possible to distinguish the intermetallic phase on the particles tracked during the whole cycle (Figure 8a-c). Additional STEM images of other particles are provided in the Supporting Information (Figure S11). During the whole cycle, after oxidation or reduction, an intermetallic phase in particles can be seen. A comparison was also performed with pure Cu particles. While Cu particles easily oxidize at relatively low temperatures (Figure S12), the intermetallic CuPt structure is substantially more robust and prevents oxidation of Cu. EELS performed on single particles revealed moderate oxidation of Cu after exposure to O2 at 800 °C. Cu was then fully reduced after re-exposure to H₂ at 800 °C, which offset the effect of O₂ exposure. To explain the drop of activity upon oxidation, one can hypothesize that Pt on the surface of the particles becomes oxidized and forms PtO or PtO₂. This causes the passivation of Pt and the drop in activity for CO oxidation. Another option could be the limited migration and oxidation of Cu on the surface upon exposure to O2, which will cover the Pt. This point will be discussed in the in situ XAS experiment shown in the next paragraph. Nevertheless, the in situ STEM analysis corroborates CO oxidation measurements shown in Figure 7. Harsh oxidation

does not destroy the intermetallic phase, which explains the easy regeneration of catalytic properties after re-reduction.

To further investigate the stability of the large CuPt particles, an in situ X-ray absorption spectroscopy experiment was performed by analyzing the X-ray near-edge structure (XANES) as well as the extended X-ray absorption fine structure (EXAFS). The Cu K and Pt L2 edges were analyzed during reduction, oxidation, and re-reduction at 800 °C, as done with the in situ STEM experiment. The results are summarized in Figure 9, with the XANES and Fourier transform (FT)-EXAFS data. The XANES and FT-EXAFS data of the Cu-K edge (Figure 9a,b) clearly show the oxidation of Cu after exposure to O₂ at 800 °C. However, re-reduction at 800 °C with H₂ reverses the changes observed after oxidation. The FT-EXAFS spectra of the Cu-K edge after reduction and re-reduction (pink and blue plots in Figure 9b) are particularly interesting, as both spectra nearly overlap. The reduced Cu data are clearly different from bulk Cu foil XANES, indicating significant alloying of Cu with Pt (Figure 9a). This is consistent with our observation with in situ STEM, which suggests a regeneration of an intermetallic structure and the reduction of Cu. The oxidation of Cu can be seen in the XANES with the decrease of a shoulder at the absorption edge at 8980 eV and the presence of a tall peak around 8995 eV (Figure 9a). In the FT-EXAFS data, a significant signal contribution for R = 1.5 Å indicates short Cu-O bonds. The Pt L2 edge was also analyzed after oxidation and re-reduction at 800 °C. The XANES and FT-EXAFS data do not suggest a substantial oxidation of Pt. Hence, the migration to the surface and the oxidation of Cu may partially prevent the oxidation of Pt after exposure to O2 at 800 °C. Based on catalytic testing on monometallic Pt particles, we inferred oxidation of Pt upon

Table 3. EXAFS Analysis Results of the Large Cu-Pt Particles Collected during the In Situ XAS Experiment^a

| | $N_{ m Cu-Cu}$ | $N_{ m Cu-Pt}$ | $N_{ m Cu-O}$ | $N_{ m Pt-Pt}$ | $R_{\text{Cu-Cu}}$ (Å) | $R_{\text{Cu-Pt}}$ (Å) | $R_{\mathrm{Cu-O}}$ (Å) | $R_{\text{Pt-Pt}}$ (Å) |
|------------|----------------|----------------|---------------|----------------|------------------------|------------------------|-------------------------|------------------------|
| fresh | 3.1 ± 1.5 | 5.8 ± 1.8 | | | 2.61 ± 0.03 | 2.65 ± 0.02 | | |
| reduced | 4.9 ± 1.9 | 5.2 ± 1.4 | | | 2.57 ± 0.01 | 2.64 ± 0.01 | | |
| oxidized | | 3.9 ± 2.8 | 2.6 ± 1.2 | 7.2 ± 3.5 | | 2.67 ± 0.03 | 1.86 ± 0.03 | 2.89 ± 0.02 |
| re-reduced | 4.0 ± 1.6 | 6.2 ± 2.2 | | | 2.57 ± 0.02 | 2.63 ± 0.03 | | |

The values of σ^2 are provided in the Supporting Information.

exposure to O_2 at 800 °C (Figure 7a shows a drop of activity after oxidation due to the formation of less active Pt oxides). We assume that copper covers Pt atoms during exposure to oxygen and ultimately prevents its oxidation.

The in situ EXAFS data were analyzed to determine the coordination numbers (N), bond lengths (R), and Debye-Waller factors of Cu-Cu, Cu-O, Cu-Pt, and Pt-Pt bonds. The experimental data were fitted with a theoretical model to estimate these parameters, and the results are summarized in Table 3. The FT-EXAFS of the data with the models for the Cu-K and Pt L2 edges are shown in Figures S13 and S14. Additional details about Debye-Waller factors and FT-EXAFS fits parameters are provided in Tables S2 and S3. The tendencies of EXAFS data are overall consistent with the behaviors shown in Figure 8 and provide an analysis on a large quantity of particles. With in situ STEM, it is only possible to investigate a small number of particles, while XAS is a bulk technique. The trend of the EXAFS data after reduction at 800 °C is compatible with the formation of an intermetallic phase. In fact, $N_{\text{Cu-Cu}}$ is close to 4, and $N_{\text{Cu-Pt}}$ is higher. After oxidation at 800 °C, Cu-O bonds of a Cu₂O phase were detected, while the coordination number for Cu-Pt bonds dropped to 3.9. This tendency indicates the partial loss of the intermetallic phase, with segregation of Cu. In addition, the results for the Pt edge are inconclusive due to Pt oxidation $(N_{\text{Pt-Pt}} \text{ is } 7.2 \text{ with a high error bar})$. After re-reduction, the Cu-Pt coordination number increased again, which suggests the remixing of Cu and Pt and is consistent with the increasing volume fraction of an intermetallic phase. Hence, we proved that the trends seen with in situ STEM are consistent using ensemble-average techniques and are well in line with changes in catalytic properties. In situ XAS confirms and complements the results seen with in situ STEM and provides an ensembleaverage investigation over a large group of particles.

CONCLUSIONS

In conclusion, we present a method to synthesize Cu-Pt nanocrystals with various sizes and crystal structures. A detailed STEM-EDS analysis of the fresh samples showed the presence of a Cu-rich core enveloped in a Pt-rich layer. STEM and XRD analysis showed the conversion of Cu-Pt particles in intermetallic CuPt particles with annealing at 800 °C. The Cu-Pt and CuPt nanoparticles are stable catalysts after exposure to oxidative or reductive environments at 400 and 800 °C, respectively. In situ STEM analysis indicates the stability of fresh non-intermetallic Cu–Pt at 400 $^{\circ}\text{C}$ under H_2 or O2. The analysis of the intermetallic phase is further refined with in situ STEM and in situ XAS. The intermetallic CuPt phase prevents substantial migration of Cu to the surface and the formation of a layer of Cu oxide, which would cover and deactivate Pt. Hence, the effect of oxidation at 800 °C with O2 can be fully reversed after a reduction with H_2 at 800 °C. This study proves that alloyed materials with Cu do not necessarily oxidize and degrade as quickly as expected and that CuPt

nanostructures can be relevant candidates to reduce the use of expensive Pt. The stability of the CuPt particles is of great interest and can be helpful for various chemical processes aside from CO oxidation.

ASSOCIATED CONTENT

Supporting Information

The Supporting Information is available free of charge at https://pubs.acs.org/doi/10.1021/jacs.2c13666.

Additional STEM and TEM images, EELS and EDS data; phase diagram for Cu-Pt; and XRD data (PDF)

AUTHOR INFORMATION

Corresponding Author

Eric A. Stach — Department of Materials Science and Engineering, University of Pennsylvania, Philadelphia, Pennsylvania 19104, United States; Laboratory for Research on the Structure of Matter, University of Pennsylvania, Philadelphia, Pennsylvania 19104, United States; orcid.org/0000-0002-3366-2153; Email: stach@seas.upenn.edu

Authors

Alexandre C. Foucher – Department of Materials Science and Engineering, University of Pennsylvania, Philadelphia, Pennsylvania 19104, United States; orcid.org/0000-0001-5042-4002

Shengsong Yang — Department of Chemistry, University of Pennsylvania, Philadelphia, Pennsylvania 19104, United States

Daniel J. Rosen — Department of Materials Science and Engineering, University of Pennsylvania, Philadelphia, Pennsylvania 19104, United States; orcid.org/0000-0003-1463-7363

Renjing Huang — Department of Chemical and Biomolecular Engineering, University of Pennsylvania, Philadelphia, Pennsylvania 19104, United States

Jun Beom Pyo – Department of Chemistry, University of Pennsylvania, Philadelphia, Pennsylvania 19104, United States

Ohhun Kwon – Department of Chemical and Biomolecular Engineering, University of Pennsylvania, Philadelphia, Pennsylvania 19104, United States; orcid.org/0000-0002-4981-1547

Cameron J. Owen — Department of Chemistry and Chemical Biology, Harvard University, Cambridge, Massachusetts 02138, United States; Occid.org/0000-0002-2543-7415

Dario Ferreira Sanchez — Paul Scherrer Institute, Villigen 5232, Switzerland

Ilia I. Sadykov – Paul Scherrer Institute, Villigen 5232, Switzerland; o orcid.org/0000-0003-1549-4771

Daniel Grolimund — Paul Scherrer Institute, Villigen 5232, Switzerland; oorcid.org/0000-0001-9721-7940

- Boris Kozinsky John A. Paulson School of Engineering and Applied Sciences, Harvard University, Cambridge, Massachusetts 02138, United States; Robert Bosch Research and Technology Center, Cambridge, Massachusetts 02139, United States; orcid.org/0000-0002-0638-539X
- Anatoly I. Frenkel Department of Materials Science and Chemical Engineering, Stony Brook University, Stony Brook, New York 11794, United States; Division of Chemistry, Brookhaven National Laboratory, Upton, New York 11973, United States; orcid.org/0000-0002-5451-1207
- Raymond J. Gorte Department of Chemical and Biomolecular Engineering, University of Pennsylvania, Philadelphia, Pennsylvania 19104, United States; orcid.org/0000-0003-0879-715X
- Christopher B. Murray Department of Materials Science and Engineering, University of Pennsylvania, Philadelphia, Pennsylvania 19104, United States; Department of Chemistry, University of Pennsylvania, Philadelphia, Pennsylvania 19104, United States

Complete contact information is available at: https://pubs.acs.org/10.1021/jacs.2c13666

Notes

The authors declare the following competing financial interest(s): One of the authors (E.A.S.) has an equity interest in Hummingbird Scientific.

ACKNOWLEDGMENTS

This work was primarily supported as part of the Integrated Mesoscale Architectures for Sustainable Catalysis (IMASC), an Energy Frontier Research Center funded by the U.S. Department of Energy, Office of Science, Basic Energy Sciences under Award #DE-SC0012573. This work was carried out in part at the Singh Center for Nanotechnology, which is supported by the NSF National Nanotechnology Coordinated Infrastructure Program under grant NNCI-2025608. Additional support to the Nanoscale Characterization Facility at the Singh Center has been provided by the Laboratory for Research on the Structure of Matter (MRSEC) supported by the National Science Foundation (DMR-1720530). The Swiss Light Source at Paul Scherrer Institute, Villigen, Switzerland, is acknowledged for beamline time at the microXAS beamline (X05LA). The authors appreciate useful discussions with Drs. O. Safonova and M. Nachtegaal.

REFERENCES

- (1) Sun, S.; Murray, C. B.; Weller, D.; Folks, L.; Moser, A. Monodisperse FePt Nanoparticles and Ferromagnetic FePt Nanocrystal Superlattices. *Science* **2000**, 287, 1989–1992.
- (2) Shevchenko, E. V.; Talapin, D. V.; Rogach, A. L.; Kornowski, A.; Haase, M.; Weller, H. Colloidal Synthesis and Self-Assembly of CoPt3 Nanocrystals. *J. Am. Chem. Soc.* **2002**, *124*, 11480–11485.
- (3) Wang, C.; Van Der Vliet, D.; Chang, K. C.; You, H.; Strmcnik, D.; Schlueter, J. A.; Markovic, N. M.; Stamenkovic, V. R. Monodisperse Pt₃Co Nanoparticles as a Catalyst for the Oxygen Reduction Reaction: Size-Dependent Activity. *J. Phys. Chem. C* **2009**, 113, 19365–19368.
- (4) Koh, S.; Strasser, P. Electrocatalysis on Bimetallic Surfaces: Modifying Catalytic Reactivity for Oxygen Reduction by Voltammetric Surface Dealloying. *J. Am. Chem. Soc.* **2007**, *129*, 12624–12625.
- (5) Bönnemann, H.; Britz, P.; Vogel, W. Structure and Chemical Composition of a Surfactant-Stabilized Pt₃Sn Alloy Colloid. *Langmuir* **1998**, *14*, 6654–6657.

- (6) Chen, H.; Chansai, S.; Xu, S.; Xu, S.; Mu, Y.; Hardacre, C.; Fan, X. Dry Reforming of Methane on Bimetallic Pt—Ni@CeO₂ Catalyst: A in Situ DRIFTS-MS Mechanistic Study. *Catal. Sci. Technol.* **2021**, *11*, 5260—5272.
- (7) López-Rodríguez, L.; Araiza, D. G.; Arcos, D. G.; Gómez-Cortés, A.; Díaz, G. Bimetallic Cu-Pt Catalysts over Nanoshaped Ceria for Hydrogen Production via Methanol Decomposition. *Catal. Today* **2021**, *11*, 5260–5272.
- (8) Kang, Y.; Murray, C. B. Synthesis and Electrocatalytic Properties of Cubic Mn-Pt Nanocrystals (Nanocubes). *J. Am. Chem. Soc.* **2010**, 132, 7568–7569.
- (9) Kang, Y.; Pyo, J. B.; Ye, X.; Gordon, T. R.; Murray, C. B. Synthesis, Shape Control, and Methanol Electro-Oxidation Properties of Pt-Zn Alloy and Pt₃Zn Intermetallic Nanocrystals. *ACS Nano* **2012**, *6*, 5642–5647.
- (10) Zhang, J.; Yang, H.; Fang, J.; Zou, S. Synthesis and Oxygen Reduction Activity of Shape-Controlled Pt₃Ni Nanopolyhedra. *Nano Lett.* **2010**, *10*, 638–644.
- (11) Rosen, D. J.; Foucher, A. C.; Lee, J. D.; Yang, S.; Marino, E.; Stach, E. A.; Murray, C. B. Microwave Heating of Nanocrystals for Rapid, Low-Aggregation Intermetallic Phase Transformations. *ACS Mater. Lett.* **2022**, *4*, 823–830.
- (12) Xin, H.; Vojvodic, A.; Voss, J.; Nørskov, J. K.; Abild-Pedersen, F. Effects of d-Band Shape on the Surface Reactivity of Transition-Metal Alloys. *Phys. Rev. B: Condens. Matter Mater. Phys.* **2014**, *89*, No. 115114.
- (13) Nørskov, J. K.; Abild-Pedersen, F.; Studt, F.; Bligaard, T. Density Functional Theory in Surface Chemistry and Catalysis. *Proc. Natl. Acad. Sci. U.S.A.* **2011**, *108*, 937–943.
- (14) Liu, Q.; Yan, Z.; Henderson, N. L.; Bauer, J. C.; Goodman, D. W.; Batteas, J. D.; Schaak, R. E. Synthesis of CuPt Nanorod Catalysts with Tunable Lengths. J. Am. Chem. Soc. 2009, 131, 5720-5721.
- (15) Zaera, F. The Surface Chemistry of Metal-Based Hydrogenation Catalysis. ACS Catal. 2017, 7, 4947-4967.
- (16) Wang, H.; Nie, X.; Chen, Y.; Guo, X.; Song, C. Facet Effect on CO₂ Adsorption, Dissociation and Hydrogenation over Fe Catalysts: Insight from DFT. *J. CO2 Util.* **2018**, *26*, 160–170.
- (17) Zhang, B.; Wang, D.; Hou, Y.; Yang, S.; Yang, X. H.; Zhong, J. H.; Liu, J.; Wang, H. F.; Hu, P.; Zhao; Yang, H. G. Facet-Dependent Catalytic Activity of Platinum Nanocrystals for Triiodide Reduction in Dye-Sensitized Solar Cells. *Sci. Rep.* **2013**, *3*, No. 01836.
- (18) Kang, Y.; Pyo, J. B.; Ye, X.; Diaz, R. E.; Gordon, T. R.; Stach, E. A.; Murray, C. B. Shape-Controlled Synthesis of Pt Nanocrystals: The Role of Metal Carbonyls. *ACS Nano* **2013**, *7*, 645–653.
- (19) Baig, N.; Kammakakam, I.; Falath, W.; Kammakakam, I. Nanomaterials: A Review of Synthesis Methods, Properties, Recent Progress, and Challenges. *Mater. Adv.* **2021**, *2*, 1821–1871.
- (20) Ghosh, S.; Manna, L. The Many "Facets" of Halide Ions in the Chemistry of Colloidal Inorganic Nanocrystals. *Chem. Rev.* **2018**, *118*, 7804–7864.
- (21) Mourdikoudis, S.; Liz-Marzán, L. M. Oleylamine in Nanoparticle Synthesis. Chem. Mater. 2013, 25, 1465–1476.
- (22) Foucher, A. C.; Yang, S.; Rosen, D. J.; Lee, J. D.; Huang, R.; Jiang, Z.; Barrera, F. G.; Chen, K.; Hollyer, G. G.; Friend, C. M.; et al. Synthesis and Characterization of Core-Shell Cu-Ru, Cu-Rh, and Cu-Ir Nanoparticles. *J. Am. Chem. Soc.* **2022**, *144*, 7919–7928.
- (23) Kang, Y.; Qi, L.; Li, M.; Diaz, R. E.; Su, D.; Adzic, R. R.; Stach, E.; Li, J.; Murray, C. B. Highly Active Pt₃Pb and Core-Shell Pt₃Pb-Pt Electrocatalysts for Formic Acid Oxidation. *ACS Nano* **2012**, *6*, 2818–2825.
- (24) Tahsini, N.; Yang, A. C.; Streibel, V.; Werghi, B.; Goodman, E. D.; Aitbekova, A.; Bare, S. R.; Li, Y.; Abild-Pedersen, F.; Cargnello, M. Colloidal Platinum-Copper Nanocrystal Alloy Catalysts Surpass Platinum in Low-Temperature Propene Combustion. *J. Am. Chem. Soc.* 2022, 144, 1612–1621.
- (25) Zhang, B. W.; Sheng, T.; Wang, Y. X.; Qu, X. M.; Zhang, J. M.; Zhang, Z. C.; Liao, H. G.; Zhu, F. C.; Dou, S. X.; Jiang, Y. X.; Sun, S. G. Platinum-Cobalt Bimetallic Nanoparticles with Pt Skin for Electro-Oxidation of Ethanol. *ACS Catal.* **2017**, *7*, 892–895.

- (26) Leteba, G. M.; Leteba, G. M.; Mitchell, D. R. G.; Levecque, P. B. J.; Macheli, L.; Van Steen, E.; Lang, C. I. High-Index Core-Shell Ni-Pt Nanoparticles as Oxygen Reduction Electrocatalysts. *ACS Appl. Nano Mater.* **2020**, *3*, 5718–5731.
- (27) Rood, S.; Eslava, S.; Manigrasso, A.; Bannister, C. Recent Advances in Gasoline Three-Way Catalyst Formulation: A Review. *Proc. Inst. Mech. Eng., Part D* **2020**, 234, 936–949.
- (28) Dey, S.; Dhal, G. C. Property and Structure of Various Platinum Catalysts for Low-Temperature Carbon Monoxide Oxidations. *Mater. Today Chem.* **2020**, *16*, No. 100228.
- (29) Fiévet, F.; Ammar-Merah, S.; Brayner, R.; Chau, F.; Giraud, M.; Mammeri, F.; Peron, J.; Piquemal, J. Y.; Sicard, L.; Viau, G. The Polyol Process: A Unique Method for Easy Access to Metal Nanoparticles with Tailored Sizes, Shapes and Compositions. *Chem. Soc. Rev.* 2018, 47, 5187–5233.
- (30) Foucher, A. C.; Marcella, N.; Lee, J. D.; Rosen, D. J.; Tappero, R.; Murray, C. B.; Frenkel, A. I.; Stach, E. A. Structural and Valence State Modification of Cobalt in CoPt Nanocatalysts in Redox Conditions. *ACS Nano* **2021**, *15*, 20619–20632.
- (31) Foucher, A. C.; Marcella, N.; Lee, J. D.; Tappero, R.; Murray, C. B.; Frenkel, A. I.; Stach, E. A. Dynamical Change of Valence States and Structure in NiCu3 Nanoparticles during Redox Cycling. *J. Phys. Chem. C* **2022**, *126*, 1991–2002.
- (32) Luneau, M.; Guan, E.; Chen, W.; Foucher, A. C.; Marcella, N.; Shirman, T.; Verbart, D. M. A.; Aizenberg, J.; Aizenberg, M.; Stach, E. A.; Madix, R. J.; et al. Enhancing Catalytic Performance of Dilute Metal Alloy Nanomaterials. *Commun. Chem.* **2020**, *3*, 1–9.
- (33) Cargnello, M.; Chen, C.; Diroll, B. T.; Doan-Nguyen, V. V. T.; Gorte, R. J.; Murray, C. B. Efficient Removal of Organic Ligands from Supported Nanocrystals by Fast Thermal Annealing Enables Catalytic Studies on Well-Defined Active Phases. *J. Am. Chem. Soc.* **2015**, *137*, 6906–6911.
- (34) Al-Shareef, R.; Harb, M.; Saih, Y.; Ould-Chikh, S.; Anjum, D. H.; Candy, J. P.; Basset, J. M. Precise Control of Pt Particle Size for Surface Structure-Reaction Activity Relationship. *J. Phys. Chem. C* **2018**, *122*, 23451–23459.
- (35) Kim, M. H.; Ebner, J. R.; Friedman, R. M.; Vannice, M. A. Determination of Metal Dispersion and Surface Composition in Supported Cu–Pt Catalysts. *J. Catal.* **2002**, *208*, 381–392.
- (36) Ringe, E.; Van Duyne, R. P.; Marks, L. D. Wulff Construction for Alloy Nanoparticles. *Nano Lett.* **2011**, *11*, 3399–3403.
- (37) Schurmans, M.; Luyten, J.; Creemers, C.; Declerck, R.; Waroquier, M. Surface Segregation in CuPt Alloys by Means of an Improved Modified Embedded Atom Method. *Phys. Rev. B* **2007**, *76*, No. 174208
- (38) Hirsimäki, M.; Lampimäki, M.; Lahtonen, K.; Chorkendorff, I.; Valden, M. Investigation of the Role of Oxygen Induced Segregation of Cu during Cu₂O Formation on Cu{1 0 0}, Ag/Cu{1 0 0} and Cu(Ag) Alloy. Surf. Sci. 2005, 583, 157–165.
- (39) Laffont, L.; Wu, M. Y.; Chevallier, F.; Poizot, P.; Morcrette, M.; Tarascon, J. M. High Resolution EELS of Cu–V Oxides: Application to Batteries Materials. *Micron* **2006**, *37*, 459–464.
- (40) Nassiri, Y.; Mansot, J. L.; Wéry, J.; Ginsburger-Vogel, T.; Amiard, J. C. Ultrastructural and Electron Energy Loss Spectroscopy Studies of Sequestration Mechanisms of Cd and Cu in the Marine Diatom Skeletonema Costatum. *Arch. Environ. Contam. Toxicol.* **1997**, 33, 147–155.
- (41) Krivanek, O. L.; Chisholm, M. F.; Nicolosi, V.; Pennycook, T. J.; Corbin, G. J.; Dellby, N.; Murfitt, M. F.; Own, C. S.; Szilagyi, Z. S.; Oxley, M. P.; Pantelides, S. T.; Pennycook, S. J. Atom-by-Atom Structural and Chemical Analysis by Annular Dark-Field Electron Microscopy. *Nature* **2010**, *464*, 571–574.
- (42) Wulff, G. XXV. Zur Frage Der Geschwindigkeit Des Wachsthums Und Der Auflösung Der Krystallflächen. Z. Kristallogr. Cryst. Mater. 1901, 34, 449–530.
- (43) Nilsson, S.; Albinsson, D.; Antosiewicz, T. J.; Fritzsche, J.; Langhammer, C. Resolving Single Cu Nanoparticle Oxidation and Kirkendall Void Formation with in Situ Plasmonic Nanospectroscopy and Electrodynamic Simulations. *Nanoscale* **2019**, *11*, 20725–20733.

- (44) Wang, W.; Dahl, M.; Yin, Y. Hollow Nanocrystals through the Nanoscale Kirkendall Effect. *Chem. Mater.* **2013**, 25, 1179–1189.
- (45) Nakamura, R.; Tokozakura, D.; Nakajima, H.; Lee, J. G.; Mori, H. Hollow Oxide Formation by Oxidation of Al and Cu Nanoparticles. *J. Appl. Phys.* **2007**, *101*, No. 074303.
- (46) Foucher, A. C.; Han, M.; Shuck, C. E.; Maleski, K.; Gogotsi, Y.; Stach, E. A. Shifts in Valence States in Bimetallic MXenes Revealed by Electron Energy-Loss Spectroscopy (EELS). 2D Mater. 2022, 9, No. 025004.
- (47) Tran, R.; Xu, Z.; Radhakrishnan, B.; Winston, D.; Sun, W.; Persson, K. A.; Ong, S. P. Surface Energies of Elemental Crystals. *Sci. Data* **2016**, *3*, 1–13.
- (48) Wen, Y. N.; Zhang, J. M. Surface Energy Calculation of the Fcc Metals by Using the MAEAM. *Solid State Commun.* **2007**, *144*, 163–167.
- (49) Abe, T.; Sundman, B.; Onodera, H. Thermodynamic Assessment of the Cu-Pt System. *J. Phase Equilib. Diffus.* **2006**, 27, 5–13.
- (50) Mao, X.; Foucher, A. C.; Montini, T.; Stach, E. A.; Fornasiero, P.; Gorte, R. J. Epitaxial and Strong Support Interactions between Pt and LaFeO₃ Films Stabilize Pt Dispersion. *J. Am. Chem. Soc.* **2020**, 142, 10373–10382.
- (51) Lin, C.; Foucher, A. C.; Ji, Y.; Curran, C. D.; Stach, E. A.; McIntosh, S.; Gorte, R. J. "intelligent" Pt Catalysts Studied on High-Surface-Area CaTiO₃ Films. *ACS Catal.* **2019**, *9*, 7318–7327.
- (52) Rodriguez, J. A.; Wayne Goodman, D. High-Pressure Catalytic Reactions over Single-Crystal Metal Surfaces. *Surf. Sci. Rep.* **1991**, *14*, 1–107.
- (53) Tahsini, N.; Yang, A.-C.; Streibel, V.; Werghi, B.; Goodman, E. D.; Aitbekova, A.; Bare, S. R.; Li, Y.; Abild-Pedersen, F.; Cargnello, M. Colloidal Platinum—Copper Nanocrystal Alloy Catalysts Surpass Platinum in Low-Temperature Propene Combustion. *J. Am. Chem. Soc.* 2022, 144, 1612—1621.
- (54) Abild-Pedersen, F.; Andersson, M. P. CO Adsorption Energies on Metals with Correction for High Coordination Adsorption Sites—A Density Functional Study. *Surf. Sci.* **2007**, *601*, 1747–1753.
- (55) Sandell, A.; Bennich, P.; Nilsson, A.; Hernnäs, B.; Björneholm, O.; Mårtensson, N. Chemisorption of CO on Cu(100), Ag(110) and Au(110). Surf. Sci. 1994, 310, 16–26.
- (56) Wegener, E. C.; Bukowski, B. C.; Yang, D.; Wu, Z.; Kropf, A. J.; Delgass, W. N.; Greeley, J.; Zhang, G.; Miller, J. T. Intermetallic Compounds as an Alternative to Single-Atom Alloy Catalysts: Geometric and Electronic Structures from Advanced X-Ray Spectroscopies and Computational Studies. *ChemCatChem* **2020**, *12*, 1325–1333.
- (57) Yang, Y.; Wei, M. Intermetallic Compound Catalysts: Synthetic Scheme, Structure Characterization and Catalytic Application. *J. Mater. Chem. A* **2020**, *8*, 2207–2221.
- (58) Yan, Y.; Du, J. S.; Gilroy, K. D.; Yang, D.; Xia, Y.; Zhang, H.; Yan, Y.; Du, J. S.; Yang, D.; Zhang, H.; Gilroy, K. D.; Xia, Y. Intermetallic Nanocrystals: Syntheses and Catalytic Applications. *Adv. Mater.* **2017**, *29*, No. 1605997.
- (59) Kresse, G. Ab Initio Molecular Dynamics for Liquid Metals. J. Non-Cryst. Solids 1995, 192–193, 222–229.
- (60) Perdew, J. P.; Burke, K.; Ernzerhof, M. Generalized Gradient Approximation Made Simple. *Phys. Rev. Lett.* **1996**, *77*, 3865.
- (61) Amaya Suárez, J.; Plata, J. J.; Márquez, A. M.; Fdez; Sanz, J. Catalytic Activity of PtCu Intermetallic Compound for CO Oxidation: A Theoretical Insight. *Catal. Today* **2022**, *383*, 339–344.
- (62) Zhang, C. J.; Baxter, R. J.; Hu, P.; Alavi, A.; Lee, M. H. A Density Functional Theory Study of Carbon Monoxide Oxidation on the Cu₃Pt(111) Alloy Surface: Comparison with the Reactions on Pt(111) and Cu(111). *J. Chem. Phys.* **2001**, *115*, 5272.
- (63) Kien, N. T.; Hashisake, K.; Chiku, M.; Higuchi, E.; Inoue, H. Activity and Durability of Intermetallic PdZn Electrocatalyst for Ethanol Oxidation Reaction. *Res. Chem. Intermed.* **2022**, *48*, 3795–3810.
- (64) Lebouil, S.; Tardelli, J.; Rocca, E.; Volovitch, P.; Ogle, K. Dealloying of Al₂Cu, Al₇Cu₂Fe, and Al₂CuMg Intermetallic Phases to

Form Nanoparticulate Copper Films. Mater. Corros. 2014, 65, 416-

T Recommended by ACS

Atomically Thick Oxide Overcoating Stimulates Low-Temperature Reactive Metal-Support Interactions for Enhanced Catalysis

Xinyu Liu, Junling Lu, et al.

MARCH 15, 2023

JOURNAL OF THE AMERICAN CHEMICAL SOCIETY

READ 🗹

Self-Assembly of Atomically Aligned Nanoparticle Superlattices from Pt-Fe₃O₄ Heterodimer Nanoparticles

Shengsong Yang, Christopher B. Murray, et al.

MARCH 13, 2023

JOURNAL OF THE AMERICAN CHEMICAL SOCIETY

READ 🗹

Facet-Controlled Synthesis of Platinum-Group-Metal Quaternary Alloys: The Case of Nanocubes and $\{100\}$ Facets

Chenxiao Wang, Younan Xia, et al.

DECEMBER 28, 2022

JOURNAL OF THE AMERICAN CHEMICAL SOCIETY

READ 🗹

Phase-Controlled Deposition of Ru on Pd Nanocrystal **Templates: Effects of Particle Shape and Size**

Annemieke Janssen, Younan Xia, et al.

JANUARY 06, 2023

THE JOURNAL OF PHYSICAL CHEMISTRY C

READ 🗹

Get More Suggestions >